Incremental capacity feature selection for lithium-ion battery state of health estimation considering estimation capability and efficiency

Cell Reports
Physical Science

Article

Incremental capacity feature selection for lithium-ion battery state of health estimation considering estimation capability and efficiency

Graphical abstract

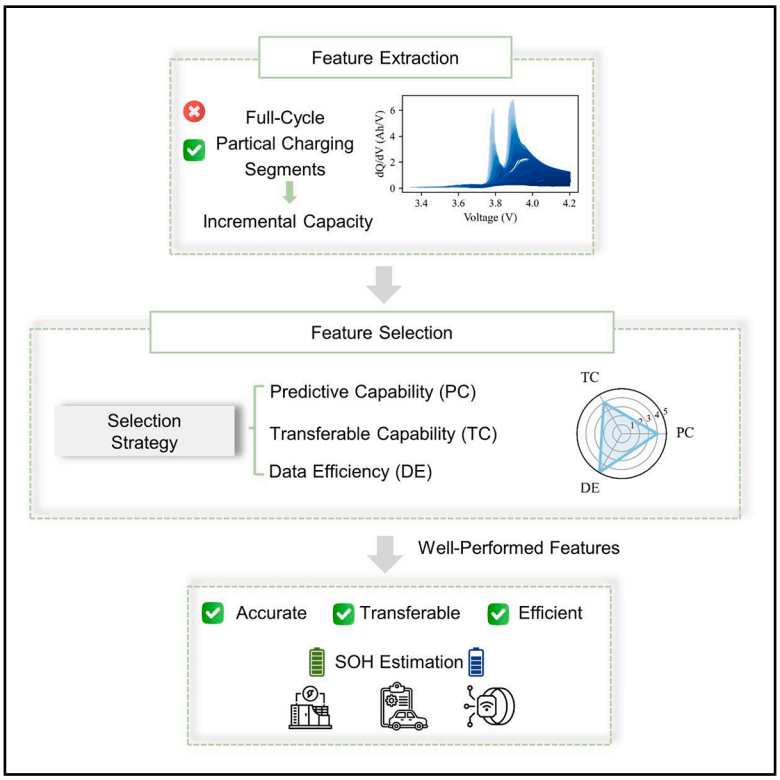

Highlights

- A unified framework evaluates feature predictability, transferability, and data efficiency
- Incremental capacity (IC) heights and peaks reflect predictability and transferability
- First IC peak enables reliable SOH estimation with less than 50% of full charging data
- The approach reduces data demands while maintaining accuracy across conditions

Authors

Lin Su (苏琳), Shengyu Tao (陶晟宇), Yingjie Chen (陈英杰), Changfu Zou (邹长福), Xuan Zhang (张璇)

Correspondence

shengyu.tao@chalmers.se (S.T.), changfu.zou@chalmers.se (C.Z.), xuanzhang@sz.tsinghua.edu.cn (X.Z.)

In brief

Su and Tao et al. present a unified evaluation of feature predictability, transferability, and data efficiency for battery health estimation. The study shows that first-peak features from incremental-capacity curves enable accurate and robust predictions using partial charging data, improving scalability while reducing data and testing requirements.

Su et al., 2026, Cell Reports Physical Science 7, 103083
February 18, 2026
https://doi.org/10.1016/j.xcrp.2025.103083

CellPress

Cell Reports
Physical Science

CellPress
OPEN ACCESS

Article

Incremental capacity feature selection for lithium-ion battery state of health estimation considering estimation capability and efficiency

Lin Su (苏琳),[1] Shengyu Tao (陶晟宇),[1,2,4,*] Yingjie Chen (陈英杰),[3] Changfu Zou (邹长福),[2,*] and Xuan Zhang (张璇)[1,*]
[1]Tsinghua Shenzhen International Graduate School, Tsinghua University, Shenzhen 518055, China
[2]Department of Electrical Engineering, Chalmers University of Technology, 41296 Gothenburg, Sweden
[3]Peking University Shenzhen Graduate School, Peking University, Shenzhen 518055, China
[4]Lead contact
*Correspondence: shengyu.tao@chalmers.se (S.T.), changfu.zou@chalmers.se (C.Z.), xuanzhang@sz.tsinghua.edu.cn (X.Z.)
https://doi.org/10.1016/j.xcrp.2025.103083

SUMMARY

Accurate and transferable estimation of battery state of health is essential for the safety and reliability of electric vehicles and energy storage systems. However, many existing approaches rely on complete charging and discharging data and overlook how feature selection, robustness, and data requirements affect estimation performance. Here, we report a unified evaluation framework for predictive capability, transferable capability, and data efficiency for five features extracted from incremental capacity curves using partial charging data. We show that the voltage and magnitude of the first peak provide a better combination of accuracy, robustness across charge rates and temperatures, and minimal data needs. We demonstrate that these two features enable accurate estimation across two datasets. The results reveal that reliable health estimation can be achieved using only the portion of charging data corresponding to roughly less than 50% of the charge process, reducing data curation effort while maintaining high accuracy and practical transferability.

INTRODUCTION

Lithium-ion batteries have been widely adopted in electric vehicles and large-scale energy storage systems, owing to their high safety performance, long cycle life, and favorable power performance.[1–4] However, batteries inevitably degrade during operation, with usable capacity and safety margins declining over time.[5] Accurate and transferable battery state of health (SOH) estimation is therefore essential to ensuring safety and reliability of these battery-enabled systems.[6,7]

State-of-the-art approaches to estimate SOH can be broadly categorized into model-based and data-driven methods. Model-based approaches, including electrochemical models and equivalent circuit models,[8–13] are limited by intrinsic complexity of coupled electrochemical and physical processes inside and between battery systems. Aging mechanisms such as loss of lithium inventory (LLI),[14–16] loss of active material (LAM),[17] and solid electrolyte interphase (SEI) growth are difficult to fully characterize over the entire life cycle, while the impedance parameters required for equivalent circuit models are labor intensive and time consuming to obtain. Moreover, the model parameters can be sensitive to different operating conditions, and it remains difficult to construct reliable models for newly designed batteries lacking full aging knowledge.

Data-driven methods have gained wide adoption with rapid advancement of artificial intelligence, offering improved simplicity and predictive accuracy. Algorithms such as support vector machines,[18] decision trees,[19] random forest,[20] relevance vector machines,[21] Gaussian process regression,[22] convolutional neural networks,[23] recurrent neural networks,[24] and long short-term memory networks[25,26] have been applied to capture statistical relationships between measured data and battery aging states.[27] For all these models, feature engineering plays a critical role, as high-fidelity and transferable features are key to accurate and transferable estimations. Widely used model inputs include voltage, current, incremental capacity (IC), and differential voltage. Among them, IC-based features have attracted particular attention because they can be obtained from partial rather than full charge or discharge data, enhancing practical feasibility. The IC, defined as the first-order derivative of capacity with respect to voltage during charging or discharging, enables extraction of features such as peak value, the corresponding voltage, and the peak area.[28,29] Li et al.[30] estimated SOH using extracted IC features in a fixed voltage range from 3.8 to 4.1 V. Lin et al.[31] proposed eight health indicators from IC, differential temperature, and differential thermal voltammetry curves to improve LSTM-based modeling. Zhao et al.[32] developed a voltage-position encoding approach that enabled robust IC-based SOH estimation from incomplete charging profiles. Moreover, the evolution of IC peak positions and heights has been shown to reflect aging mechanisms,[33] providing a strong physical basis for feature and machine learning model interpretation.

Many studies use feature selection methods to enhance model performance, with particular attention to the correlation

Please cite this article in press as: Su et al., Incremental capacity feature selection for lithium-ion battery state of health estimation considering estimation capability and efficiency, Cell Reports Physical Science (2025), https://doi.org/10.1016/j.xcrp.2025.103083

between features and SOH. For example, Li et al. applied gray relation analysis to quantify the correlation between health indicators and battery capacity, and used this as the basis for model variable selection.[34] Marri et al. extracted features from charging curves under different voltage limits and ranges, and analyzed their linear dependence with capacity reduction.[35] Li et al. further proposed a systematic feature selection approach that evaluated features through multi-model influence factor scoring.[36] Beyond correlation-based selection, several studies also consider robustness under varying operating conditions. Wei et al. ranked features using random forest importance and introduced an MSHHO algorithm to avoid local optima.[37] Xia et al. adopted a sequential forward selection strategy combined with multi-objective optimization to extract features from impedance spectroscopy, reducing feature size and eliminating irrelevant information.[38] Although these approaches improve feature performance, they might overlook the cost of feature acquisition. Tao et al. demonstrated that features extracted from the first 120 cycles can be seen as sufficient for some battery management tasks, as adding more data did not improve estimation accuracy.[39] Wang et al. designed an automatic feature selection pipeline that reduced 206 raw features to a few features, improving the data efficiency of the trained model.[40] However, existing research lacks a systematic consideration of predictive capability (PC), transferable capability (TC), and data efficiency (DE) of the feature engineering process. Although numerous features have been proposed in recent years and proven effective for battery diagnostics, their accuracy and robustness across different conditions are still uncertain. This gap is crucial because feature effectiveness directly affects the efficiency, interpretability, and transferability of algorithmic decisions in practical battery management systems. As a result, many existing extracted features perform well under specific operating conditions or contain excessive information redundancy, leading to low data efficiency and reduced generalizability. To sum up, several critical issues remain unresolved: (1) features with high PC across different operating conditions remain under-investigated, and TC of extracted features is not well identified, and (2) the critical balance between DE and model predictive accuracy is under-investigated, as model accuracy is often prioritized while data acquisition and model training costs are frequently neglected. These gaps highlight the urgent need for unified PC, TC, and DE evaluation methods that are critically important to achieve scientifically grounded feature selection and maximize data efficiency.

This work extracts five features from IC curves and proposes three criteria: PC, TC, and DE. PC is defined as the ability of features to accurately reflect SOH, quantified through correlation analysis. TC captures the contribution of features to cross-condition SOH prediction, using the differences between SHAP-based and correlation-based feature importance rankings. DE emphasizes achieving sufficient estimation accuracy with the least number of features, thereby reducing testing time and data redundancy. Based on correlation, interpretability, and sensitivity analyses, we demonstrate that two features, the horizontal and vertical coordinates of the first IC peak, can be seen as sufficient for accurate SOH estimation across the studied operating conditions. This result indicates the potential to avoid unnecessary data curation and feature redundancy. An XGBoost-based model is employed for SOH prediction, and the framework is validated on CALCE and TJU datasets, spanning 24 batteries with 2 chemistry types over 6,000 cycles. Specifically, a transfer learning based on fine-tuning is performed from 1C to 0.5C discharge batteries in the CALCE dataset and from 25°C to 35°C batteries in the TJU dataset. Notably, with these two features (the x- and y-coordinates of the first peak), the CALCE dataset achieves an SOH estimation mean absolute percentage error (MAPE) of 4.82%, while the TJU dataset reaches a 0.65% MAPE with high accuracy and robustness. This work highlights both the technical and economic potential of PC, TC, and DE analysis when developing data-driven battery management algorithms, especially considering accuracy, transferability, and computational resource constraints.

RESULTS

Datasets and feature extraction

Two datasets encompassing batteries under different test conditions are employed in this study. They are summarized in Table S1. Furthermore, the proposed method is equally applicable to datasets with diverse test conditions. The first dataset[41] is from the Center for Advanced Life Cycle Engineering (CALCE) at the University of Maryland. Charging was performed using a constant-current (CC) mode at 0.5C until the voltage reached 4.2 V, followed by a constant-voltage (CV) phase at 4.2 V until the current dropped below 0.05 A. Discharging was conducted under CC mode with a cut-off voltage of 2.7 V. In this dataset, CS_35 batteries served as the source domain (discharged at 1C), while CS_33 batteries served as the target domain (discharged at 0.5C).

The second dataset[42] is from Tongji University (TJU) and contains 18650-type NCA batteries tested at 25°C, 35°C, and 45°C. Batteries tested at 25°C and 35°C are used in this work. The source domain includes 19 batteries charged at 0.5C and discharged at 1C at 25°C, while the target domain includes 3 batteries charged at 0.5C and discharged at 1C at 35°C.

Both CALCE and TJU datasets follow the CC-CV charging protocol. Incremental capacity (IC) curves were derived by plotting dQ/dV against voltage, as shown in Figure 1. Multiple features were extracted from the IC curves, including the x- and y-coordinates of the first peak (P1_x, P1_y), the x- and y-coordinates of the second peak (P2_x, P2_y), and the area under the curve between the two peaks (P12_Ar). Figures 1A and 1B present the IC curves of the CALCE dataset in the source and target domains, respectively, where light blue denotes the early aging stages and dark blue corresponds to the later stages. The lifetimes of the source-domain battery CS_35 and the target-domain battery CS_33 are 870 and 850 cycles, respectively. Figures 1C and 1D illustrate the IC curves of the TJU dataset using the longest-lived batteries in the source and target domains (210 and 570 cycles, respectively) as representative examples. As cycling progresses, the voltage increases, the IC heights decrease, and the area enclosed by the IC curve becomes smaller. This demonstrates that IC curves capture aging information, which can be exploited through feature extraction.

Please cite this article in press as: Su et al., Incremental capacity feature selection for lithium-ion battery state of health estimation considering estimation capability and efficiency, Cell Reports Physical Science (2025), https://doi.org/10.1016/j.xcrp.2025.103083

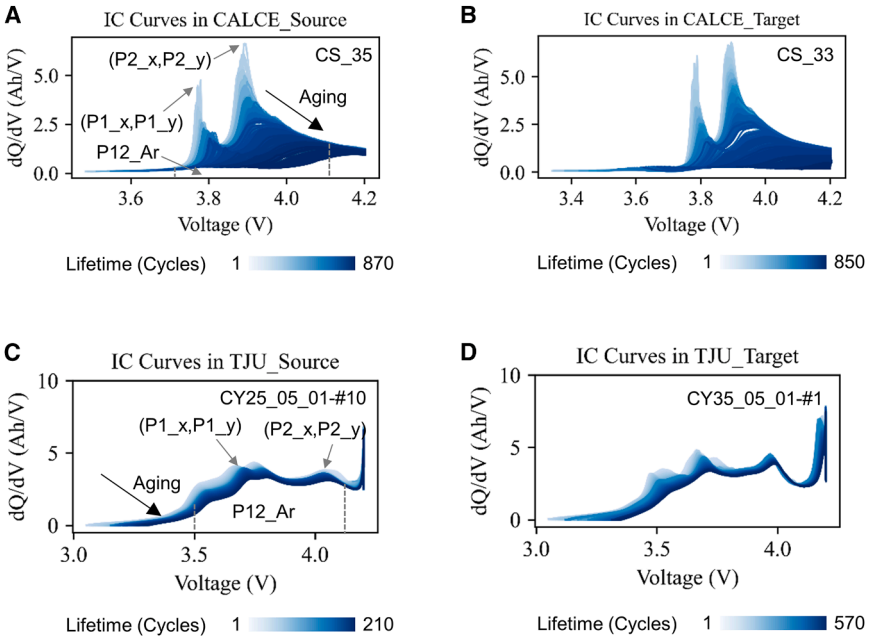

Figure 1. Incremental capacity curves of the two datasets

(A) Incremental capacity (IC) curves of the CALCE source domain (discharge rate: 1C), where the *x* axis represents the charging voltage and the *y* axis denotes the ratio of charging capacity to voltage; the color transition from light to dark blue indicates battery aging from 1 to 870 cycles.

(B) IC curves of the CALCE target domain (discharge rate: 0.5C), where the *x* axis represents the charging voltage and the *y* axis denotes the ratio of charging capacity to voltage; the color transition from light to dark blue indicates battery aging from 1 to 850 cycles.

(C) IC curves of the TJU source domain (25°C, charge rate: 0.5C), where the *x* axis represents the charging voltage and the *y* axis denotes the ratio of charging capacity to voltage; the color transition from light to dark blue indicates battery aging from 1 to 210 cycles.

(D) IC curves of the TJU target domain (35°C, charge rate: 0.5C), where the *x* axis represents the charging voltage and the *y* axis denotes the ratio of charging capacity to voltage; the color transition from light to dark blue indicates battery aging from 1 to 570 cycles.

The feature names and explanations are presented in Table S2. Figure 2 shows the evolution of each feature value with cycling. Figures 2A–2E illustrate the trajectories of five features for the CALCE target-domain battery CS_33, while Figures 2F–2J present the corresponding results for the TJU target-domain battery #1. Among these features, P1_x and P2_x exhibit an increasing trend with cycle number, whereas P1_y, P2_y, and P12_Ar display a decreasing trend.

Feature predictive capability

The purpose of feature extraction is to construct a data space from existing measurements that can accurately predict the SOH. To assess the predictive capability of each feature, we calculated the correlation between individual features and SOH. A higher correlation indicates a stronger mapping relationship and better predictive potential. Figure 3 presents the correlation analysis for two datasets. Figures 3A and 3B show the heatmaps of feature–SOH correlations for the source and target domains of the CALCE dataset, respectively. Among all features, P12_Ar, P1_x, and P2_x exhibit the highest correlation coefficients, with values of 0.99, −0.95, and 0.98 in the source domain, and 0.96, −0.97, and −0.98 in the target domain, consistently ranking among the top three. Figures 3C and 3D present the corresponding results for the TJU dataset. In this case, P12_Ar also demonstrates a strong correlation with SOH. Although the correlation of P2_x decreases, P1_x retains a relatively high correlation with SOH. In addition, the Spearman correlation coefficient is used to analyze the relationship between the features and SOH degradation (Figure S1). The Spearman coefficients of P1_y and P2_y are higher than their Pearson correlation, which suggests that peak-related features are more effective in capturing non-linear relationships, especially under complex influencing factors. This supports the contribution of P1_y and P2_y to transferability under different operating conditions.

Feature transferable capability

Correlation analysis reflects the predictive capability of features within a single dataset. However, it does not reveal whether these features can still accurately estimate SOH under varying operating conditions. To address this limitation, we further evaluate the transferable capability of features. XGBoost is employed as the predictive model for cross-domain learning, and SHAP analysis is used to interpret feature contributions. This approach provides a combined assessment of both PC and TC. If a feature shows high importance in the XGBoost model but relatively low correlation with the target variable, it suggests that the feature may contain information that the model can capture but is not easily revealed through simple correlation analysis. Such information is likely to possess strong transferability, as it may reflect more intrinsic and cross-task feature patterns within the data. Figure 4A presents the SHAP analysis for the CALCE dataset under cross-condition SOH prediction. The highest-ranked feature is P2_y, which represents the vertical coordinate of the second peak. Compared with correlation analysis, the feature rankings change under SHAP analysis because SHAP is model-based and accounts for both PC and TC. Since cross-domain prediction is considered, the ranking shifts can reflect TC. A feature that moves upward in the ranking indicates higher TC, whereas a downward shift suggests lower TC, which may hinder SOH estimation under varying battery conditions. To quantify TC, we calculate the difference between SHAP-based and correlation-based rankings in Figure 4B. Features P1_y and P2_y show positive ranking changes of 1 and 3, respectively, indicating higher TC, while the horizontal features P1_x and P2_x show little or negative change. Similarly, Figure 4C displays the SHAP analysis for the TJU dataset. Here, P1_y ranks first and P2_y ranks third. In Figure 4D, the ranking differences again confirm that P1_y and P2_y exhibit positive changes (both +1), whereas P1_x shows a negative shift. An additional validation

CellPress
OPEN ACCESS

Cell Reports
Physical Science
Article

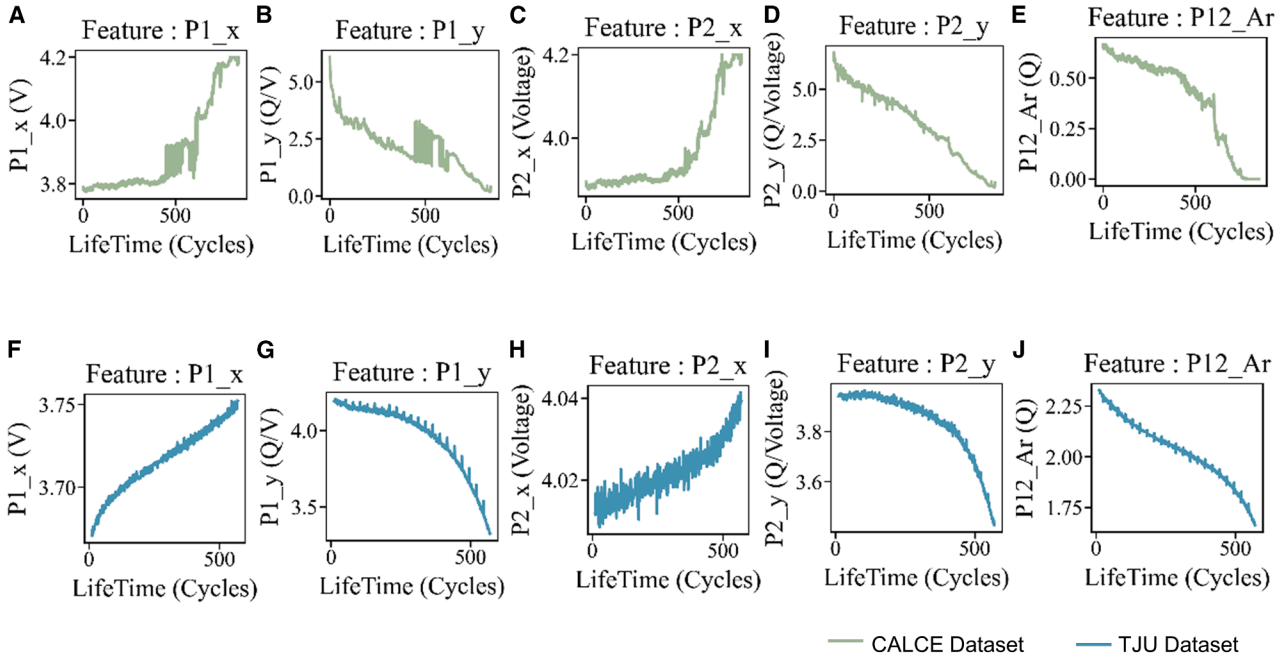

Figure 2. The feature curves of the CALCE and TJU datasets

(A–E) Feature curves of battery CS_33 in the CALCE dataset.

(F–J) Feature curves of battery #1 in the TJU dataset.

using the Oxford battery dataset, which differs in material composition from the CALCE and TJU datasets, further confirms the same trend (Table S3).

Feature data efficiency

The use of more features does not necessarily lead to better performance. Instead, an appropriate number of features should be selected while considering the time required to obtain them, thereby ensuring data efficiency. As charging progresses, more features become available as the state of charge (SOC) increases. Once SOC reaches 1, all SOH-related information can be captured, but this results in substantial data acquisition time and energy consumption. To evaluate the trade-off between feature quantity and prediction performance, we conduct a

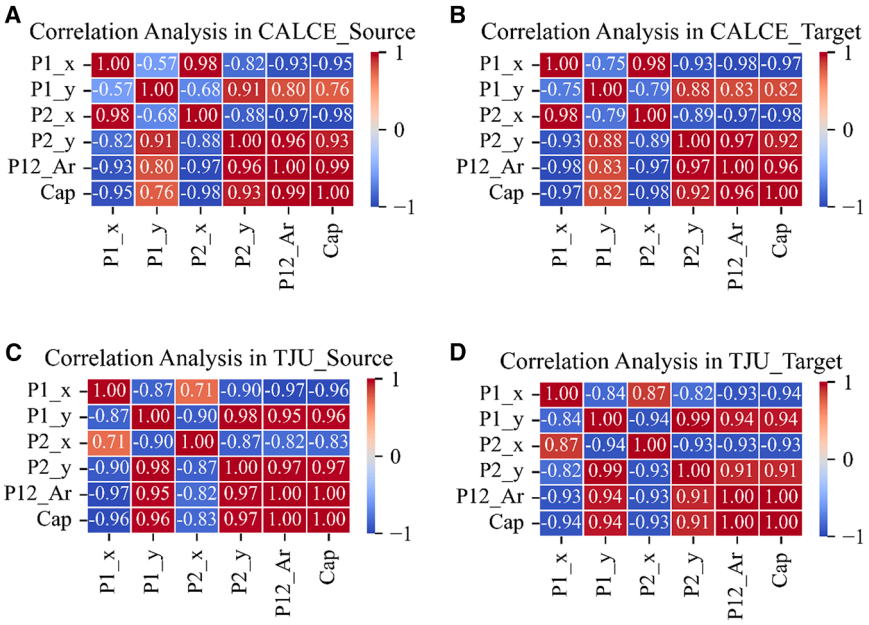

Figure 3. Feature predictive capability analysis of the two datasets

(A) Heatmap of feature predictive capability (PC) for the CALCE source domain (discharge rate: 1C).

(B) Heatmap of feature PC for the CALCE target domain (discharge rate: 0.5C).

(C) Heatmap of feature PC for the TJU source domain (25°C).

(D) Heatmap of feature PC for the TJU target domain (35°C).

Please cite this article in press as: Su et al., Incremental capacity feature selection for lithium-ion battery state of health estimation considering estimation capability and efficiency, Cell Reports Physical Science (2025), https://doi.org/10.1016/j.xcrp.2025.103083

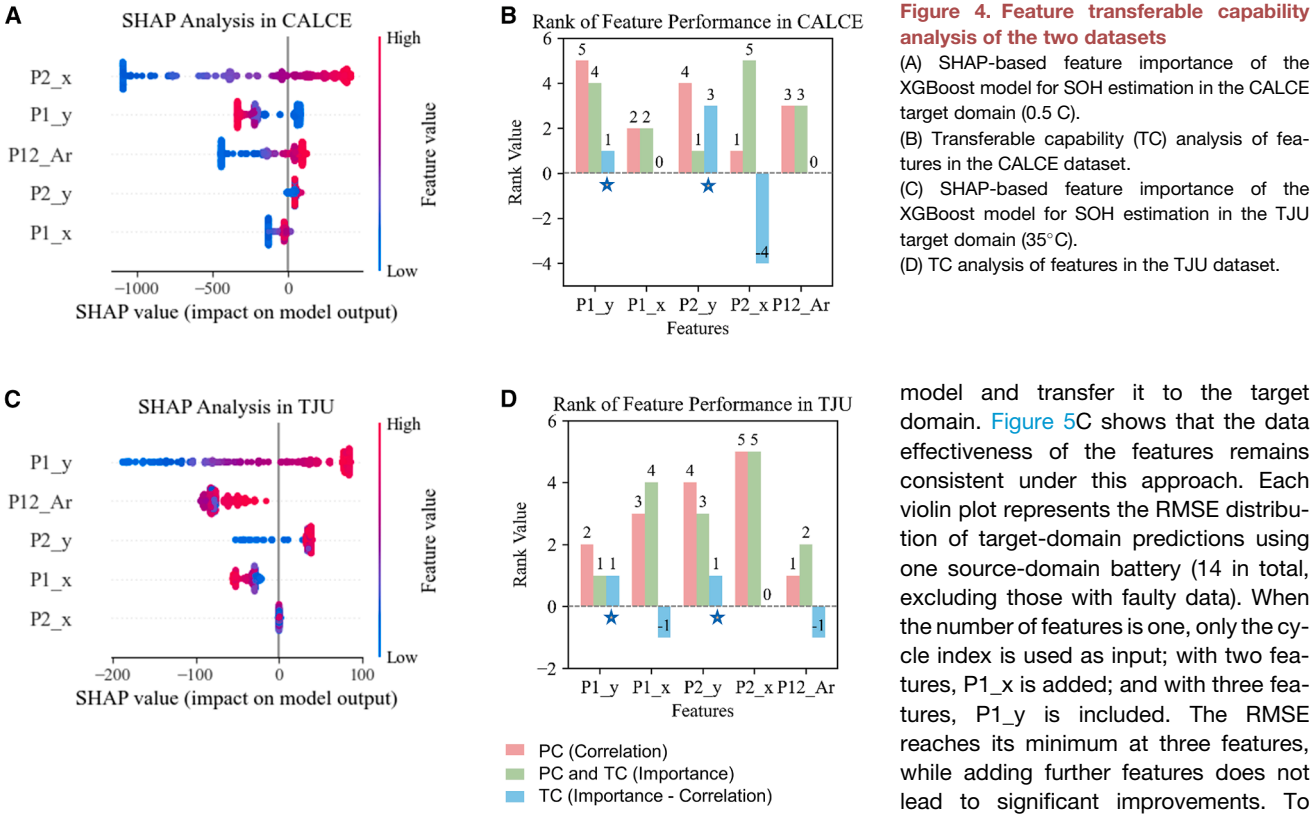

Figure 4. Feature transferable capability analysis of the two datasets

(A) SHAP-based feature importance of the XGBoost model for SOH estimation in the CALCE target domain (0.5 C).

(B) Transferable capability (TC) analysis of features in the CALCE dataset.

(C) SHAP-based feature importance of the XGBoost model for SOH estimation in the TJU target domain (35°C).

(D) TC analysis of features in the TJU dataset.

sensitivity analysis by incrementally adding features in the order they become available, starting with the first peak, followed by the second peak, and then features beyond the second peak. For each feature combination, the root-mean-square error (RMSE) and mean absolute error (MAE) of SOH in the target domain are calculated.

Figure 5A shows the feature data efficiency analysis for the CALCE dataset. The cycle number was first used as the initial feature input, as it has an inherent relationship with SOH evolution. Subsequently, features P1_x, P1_y, P2_x, P2_y, and P12_Ar are added sequentially. The estimation error decreases sharply with the addition of the first few features and then only slightly thereafter. A clear inflection point occurs at three features, indicating that the two features from the first peak are sufficient to achieve high prediction accuracy. The occurrence of the inflection point is consistent across different data samples, indicating that it is stable. Similarly, Figure 5B presents the results for the TJU dataset, where the RMSE decreases sharply at first but shows slight fluctuations when more than three features are included. The MAE decreases gradually after the addition of P1_x and P1_y. This again suggests that the features from the first peak alone are sufficient for accurate SOH estimation. The robustness analysis with different proportions of target domain data is shown in Figures S2 and S3. In addition, this finding is further validated on the Oxford dataset different from existing material compositions and transfer conditions (Table S4). Selecting only one source battery may introduce subjectivity. Therefore, each source battery is used to train the model and transfer it to the target domain. Figure 5C shows that the data effectiveness of the features remains consistent under this approach. Each violin plot represents the RMSE distribution of target-domain predictions using one source-domain battery (14 in total, excluding those with faulty data). When the number of features is one, only the cycle index is used as input; with two features, P1_x is added; and with three features, P1_y is included. The RMSE reaches its minimum at three features, while adding further features does not lead to significant improvements. To assess the model's practicality and computational efficiency in real-world applications, the model size, training time, and prediction time obtained using these three features are reported in Table S5. In addition to considering individual source batteries, it is also necessary to examine the impact of increasing the number of source batteries on SOH estimation. When multiple source batteries are available, they are combined for training and the RMSE is evaluated. As shown in Figure 5D, the RMSE varies with both the feature combination and the number of source batteries, dropping sharply when three features and two source batteries are used. However, when the number of source batteries exceeds two, the RMSE remains nearly unchanged. In addition, the validation results on the Oxford dataset also demonstrate that both the appropriate number of features and the number of source-domain batteries contribute significantly to the reduction of RMSE (Figure S4).

Analysis of predictive and transferable capability and data efficiency

A comprehensive analysis of PC, TC, and DE is conducted for each individual feature as well as for different feature combinations. Figure 6 presents the evaluation results across these three dimensions, together with the corresponding SOH estimation. The SOH estimation errors, including MAE, MSE, and MAPE, are summarized in Table 1. The values of PC and TC are derived from feature ranking, whereas DE is assigned based on acquisition time: features from the first peak, the second peak, and those involving both peak areas are given scores of 5, 3, and 1, respectively. Figures 6A–6E show that

Please cite this article in press as: Su et al., Incremental capacity feature selection for lithium-ion battery state of health estimation considering estimation capability and efficiency, Cell Reports Physical Science (2025), https://doi.org/10.1016/j.xcrp.2025.103083

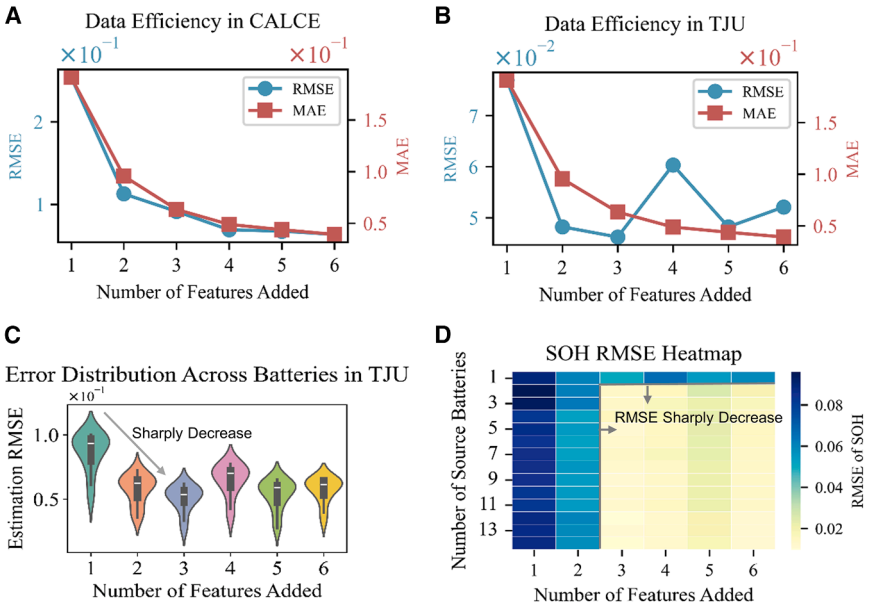

Figure 5. Feature data efficiency (DE) of the two datasets

(A) Sensitivity analysis of feature combinations for the CALCE target domain, where the *x* axis represents the cumulative number of included features, and the *y* axis shows the root mean squared error (RMSE) and mean absolute error (MAE) of SOH estimation.

(B) Sensitivity analysis of feature combinations for the TJU target domain, with the same axis definitions as in (A).

(C) Sensitivity analysis for the TJU target domain considering different source-domain batteries. For each feature combination, the model is trained on each individual source battery and transferred to the target battery. Each violin plot represents the distribution across multiple source batteries.

(D) Heatmap of SOH RMSE across different feature combinations and numbers of source batteries, where color intensity indicates error magnitude.

each feature exhibits distinct strengths and limitations across the three dimensions. For example, P1_x demonstrates high PC and DE but relatively low TC, whereas P2_y exhibits high TC but low PC and DE. In general, horizontal-axis features tend to yield higher PC, while vertical-axis features show higher TC. Features related to the first peak generally provide better DE, while those requiring longer acquisition times are associated with lower DE. In terms of SOH estimation, P12_Ar achieves the highest accuracy, yielding an MAPE of only 0.22%, but obtaining this feature requires extended measurement. In contrast, using P1_x and P2_y individually results in MAPE values of 1.84% and 2.52%, respectively, while P2_x and P2_y produce higher errors of 7.61% and 10.26%. Figures 6F–6I further illustrate the analysis of feature combinations. Combination 1 provides balanced performance across all three dimensions, achieving an SOH estimation MAPE of only 0.65%. By contrast, combinations 2, 3, and 4 show relatively high PC and TC but low DE, leading to larger MAPE values of 1.62%, 2.50%, and 1.43%, respectively. In addition to the radar chart plotted based on rankings, the radar chart calculated from the numerical indicators of PC, TC, and DE is provided in Table S6 and Figure S5.

SOH estimation

Figure 7 presents the SOH estimation results on the CALCE and TJU datasets using different numbers of source batteries, with comparisons between using all features and only two key features.

Figure 7A shows the SOH estimation results for the CALCE target domain. When only the first-peak features are used for estimation and transfer, the predicted SOH remains close to the ground truth, showing only minor deviations from the results obtained with all features and even achieving higher accuracy at later stages. Figure 7B displays the corresponding absolute estimation errors, where using only the first-peak features yields lower errors. The estimation errors (MAE, RMSE, and MAPE) obtained with the P1 features (P1_x and P1_y) are 0.0339, 0.0461, and 4.82%, respectively, as reported in Table 2.

Figure 7C illustrates SOH estimation for the TJU target domain using a single source battery. A random seed of 55 is set, and ten runs are performed, each time randomly selecting one source battery. The results obtained under other random seeds are provided in Table S7 and Figure S6. The average of the ten estimates is plotted as SOH results, and the standard deviation is calculated to construct the error band. Across different feature combinations, SOH estimated with only the first-peak features remains closer to the ground truth than with all features. Figure 7D presents the corresponding absolute errors, again showing smaller deviations when only the first-peak features are used. The prediction errors (MAE, RMSE, and MAPE) with the P1 features are 0.0059, 0.0070, and 0.65%, respectively, as listed in Table 3, all of which are significantly lower than those obtained with all features. Figures 7E and 7F show the SOH estimation results and absolute errors when two source batteries are used. A random seed of 55 is set, and 10 runs are performed, each time randomly selecting two source batteries. The ten estimates are averaged, and the standard deviation is calculated to construct the error band. Compared with the case of using a single source battery, the SOH predictions are closer to the ground truth. The prediction errors (MAE, RMSE, and MAPE) with the P1 features are 0.0059, 0.0068, and 0.65%, respectively, as reported in Table S8, again significantly lower than those obtained with all features.

Finally, Figures 7G and 7H show the results and errors when three source batteries are used. A random seed of 55 is set, and ten runs are performed, each time randomly selecting three source batteries. To better capture battery behavior under high-temperature conditions and to provide a more challenging transfer scenario, the SOH estimation and corresponding errors at

Cell Reports
Physical Science
Article

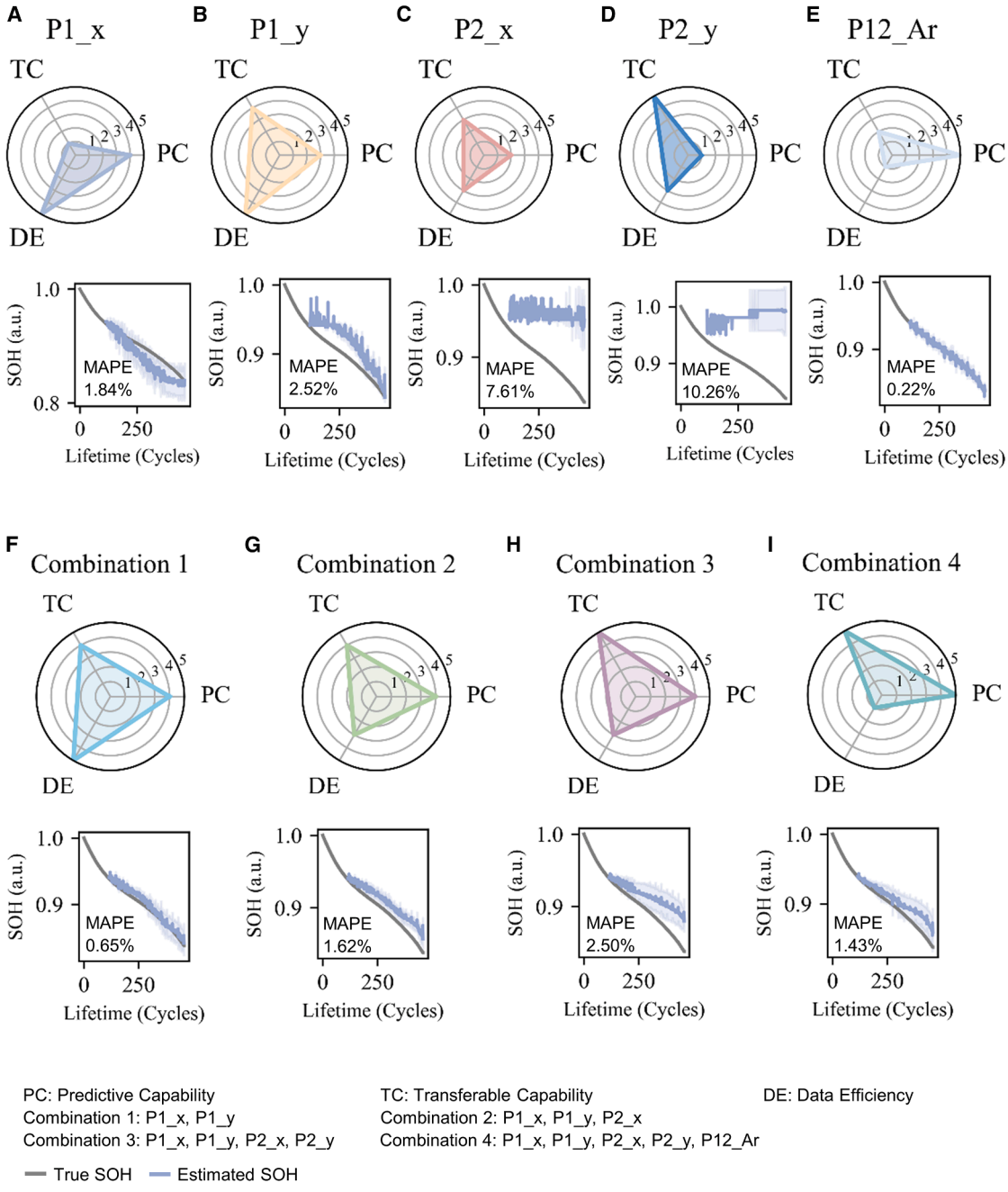

Figure 6. Comprehensive analysis of PC, TC, and DE

(A–E) Analysis of the PC, TC, and DE of a single feature, along with their SOH estimation results.

(F–I) Analysis of the PC, TC, and DE of combined features, along with their SOH estimation results.

45°C are presented in Figure S7. The average results are plotted as SOH, and standard deviation is used to construct the error band. The prediction errors (MAE, RMSE, and MAPE) with the P1 features are 0.0071, 0.0078, and 0.80%, respectively, as reported in Table S9, all significantly lower than the errors obtained with all features. The error distribution shown in Figure 7 is provided in Table S10.

METHODS

IC curve smoothing and feature extraction

To extract reliable features from the IC curves, the raw voltage-capacity data are first smoothed using the Savitzky-Golay filter to suppress measurement noise while preserving the curve's peak shape. Let $Q(t)$ and $V(t)$ denote the charge capacity and

Table 1. SOH estimation error under different features and feature combinations

	P1_x	P1_y	P2_x	P2_y	P12_Ar	Com1	Com2	Com3	Com4
MAE	0.0163	0.0225	0.0671	0.0904	0.0020	0.0059	0.0143	0.0219	0.0125
RMSE	0.0192	0.0243	0.0716	0.0974	0.0028	0.0068	0.0153	0.0249	0.0147
MAPE	1.84%	2.52%	7.61%	10.26%	0.22%	**0.65%**	1.62%	2.50%	1.43%

voltage as functions of time during the charging step. The IC curve is defined as:

$$\frac{dQ}{dV} = \frac{\frac{dQ}{dt}}{\frac{dV}{dt}} \quad \text{(Equation 1)}$$

Both $Q(t)$ and $V(t)$ are smoothed using the Savitzky-Golay filter, which fits a polynomial of degree p within a moving window of width w to minimize least squares error. p is 3 in this study. The smoothed value is computed as:

$$\hat{y}(n) = \sum_{k=-m}^{m} c_k y(n+k) \quad \text{(Equation 2)}$$

Where $\hat{y}(n)$ is the value of the smoothed signal at the n-th sampling point, c_k is the convolution coefficient derived from the local

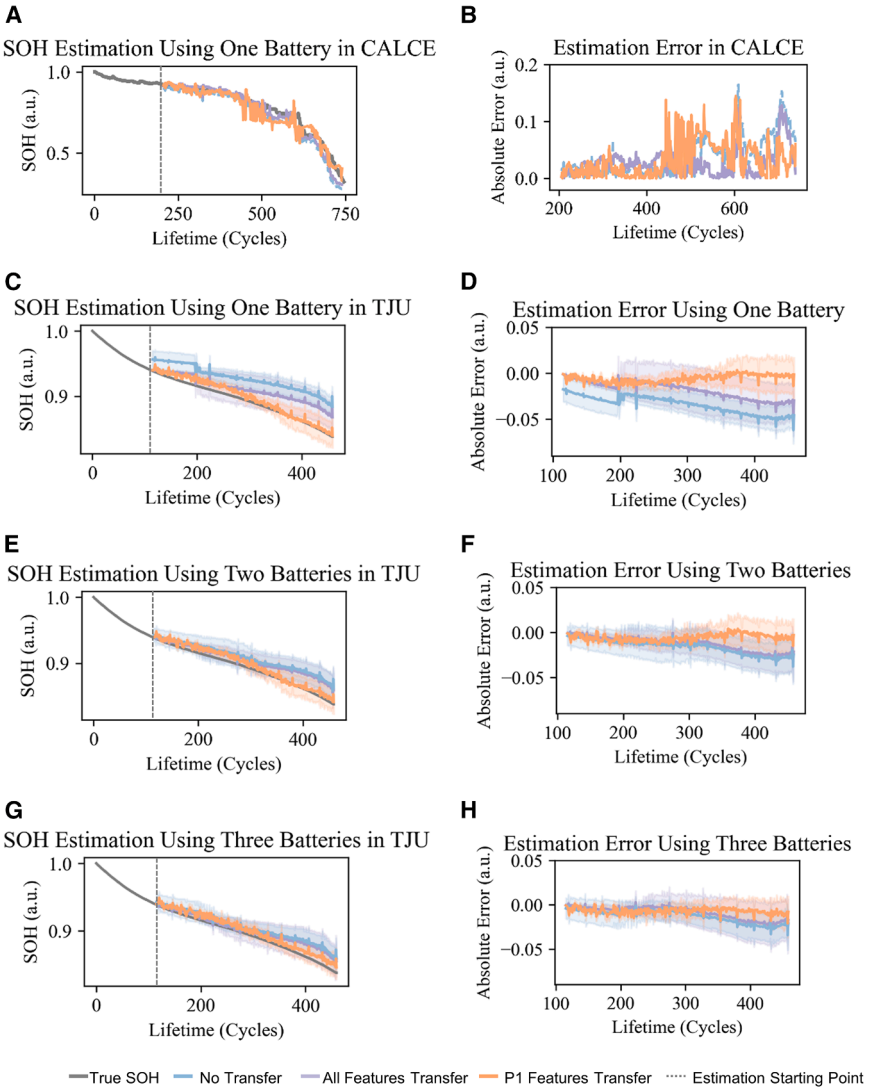

Figure 7. SOH estimation results for the two datasets under different transfer settings

(A and B) Comparison of SOH estimation and absolute errors in the CALCE target domain without transfer learning, with full feature transfer, and with transfer based on only the first peak feature.

(C and D) Comparison of SOH estimation and absolute errors in the TJU target domain using one battery from the source domain, without transfer learning, with full feature transfer, and with transfer based on only the first peak feature.

(E and F) Comparison of SOH estimation and absolute errors in the TJU target domain using two batteries from te source domain, without transfer learning, with full feature transfer, and with transfer based on only the first peak feature.

(G and H) Comparison of SOH estimation and absolute errors in the TJU target domain using three batteries from the source domain, without transfer learning, with full feature transfer, and with transfer based on only the first peak feature.

Table 2. SOH estimation error in CALCE, with no transfer, all features transfer, and only P1 features transfer

	MAE	RMSE	MAPE	R^2
No transfer	0.0406	0.0536	6.43%	0.8647
All features + transfer	0.0281	0.0365	4.24%	0.8996
P1 features + transfer	**0.0339**	**0.0461**	**4.82%**	**0.9371**

polynomial fit, $m = \frac{w-1}{2}$, m is the window half-size, and w is chosen as an odd number which is 21 to ensure symmetry. The filtered IC curve $\frac{dQ}{dV}(V)$ reveals local peaks that correspond to distinct electrochemical phase transitions, from which characteristic features are subsequently extracted.

Predictive capability

The correlation between features and capacity reflects the degree to which a feature can accurately predict capacity, with stronger correlations indicating a higher potential for reliable capacity representation. Thus, we define predictive capability (*PC*) using the Pearson correlation coefficient:

$$PC_i = \frac{\sum_{j=1}^{m}\left(F_i^j - \overline{F}_i\right)\left(SOH^j - \overline{SOH}\right)}{\sqrt{\sum_{j=1}^{m}\left(F_i^j - \overline{F}_i\right)^2 \sum_{j=1}^{m}\left(SOH^j - \overline{SOH}\right)^2}} \quad \text{(Equation 3)}$$

$$SOH = \frac{Capacity_{current}}{Capacity_{initial}} \quad \text{(Equation 4)}$$

Where, PC_i denotes the correlation coefficient of the i-th feature, F_i^j is the value of the i-th feature at the j-th cycle, SOH^j is the corresponding ratio of capacity to initial capacity, and m is the number of lifetime cycles. The averages of features and capacity are given by:

$$\overline{F}_i = \frac{1}{m}\sum_{j=1}^{m} F_i^j \quad \text{(Equation 5)}$$

$$\overline{SOH} = \frac{1}{m}\sum_{j=1}^{m} SOH^j \quad \text{(Equation 6)}$$

Transferable capability

To evaluate whether extracted features are not only predictive within a single dataset but also transferable across domains, the TC of features is introduced. The underlying principle is that a transferable feature shows greater importance in model-based interpretability than in correlation-based analysis, because model interpretability statistically reflects how well or how stably a feature contributes to specific SOH estimation results across different domains as compared with other features, which essentially represents TC. The interpretability-based importance of the i-th feature is obtained by training an XGBoost model (explained in a later section), from which the relative contribution of each feature to the model output is derived.

Table 3. SOH estimation error in TJU using one battery from the source domain, with no transfer, all features transfer, and only P1 features transfer

	MAE	RMSE	MAPE	R^2
No transfer	0.0343	0.0355	3.87%	−0.6856
All feature transfer	0.0180	0.0203	2.05%	0.4475
P1 feature transfer	**0.0059**	**0.0070**	**0.65%**	**0.9341**
Error reduction rate (compared to all features)	67.2%	65.5%	68.3%	–
Error reduction rate (compared to no transfer)	82.8%	80.3%	83.2%	–

The ranking position of the i-th feature in this model-based importance evaluation is denoted as R_i^{model}. It is calculated using the SHAP value

The SHAP value of the i-th feature for a given sample x is defined as:

$$\Phi_i(f,x) = \sum_{S\subseteq F\setminus\{i\}} \frac{|S|!(|F| - |S| - 1)!}{|F|!}\left[f_{S\cup\{i\}}(x_{S\cup\{i\}}) - f_S(x_S)\right] \quad \text{(Equation 7)}$$

Where F denotes the complete set of features, $S\subseteq F\setminus\{i\}$is any subset of features that does not contain feature i, and $f(\cdot)$ is the predictive model. The global importance of feature i is obtained as the expectation of the absolute SHAP values over all samples:

$$I_i^{SHAP} = \mathbb{E}_x[|\Phi_i(f,x)|] \quad \text{(Equation 8)}$$

Based on this definition, the model-based ranking position of feature i is given by:

$$R_i^{model} = rank\left(I_i^{SHAP}\right) \quad \text{(Equation 9)}$$

In parallel, the correlation-based PC defined in Section 2.1 provides another ranking of features, denoted as R_i^{corr}:

$$R_i^{corr} = rank(PC_i) \quad \text{(Equation 10)}$$

The TC of the i-th feature is then defined as:

$$TC_i = R_i^{corr} - R_i^{model} \quad \text{(Equation 11)}$$

A larger difference indicates that a feature receives a higher ranking when model-based importance, which incorporates both TC and PC, is considered. This suggests higher transferability in cross-domain SOH estimation. In contrast, a smaller difference implies that the feature's ranking decreases after accounting for TC and PC, indicating lower transferability in cross-domain SOH estimation.

Data efficiency

The data efficiency of feature utilization during SOH estimation is examined through a progressive feature addition strategy designed to emulate the process of gradually acquiring information along the charging trajectory. Beginning with the most

fundamental cycling index, features are incorporated according to their difficulty of acquisition, thereby forming a series of nested feature sets. The feature subset is expressed as: $F_k = \{f_1, f_2, \cdots, f_k\}, k = 1,2,\cdots,N$.

Where, f_k denotes the k-th selected feature, and N is the maximum number of features considered. For each subset F_k, source-domain data are used to train an XGBoost model, and the trained model is subsequently applied to the target-domain battery. The output is the estimated SOH of the target battery. The estimation error is quantified using the RMSE and MAE, which are defined in Section 2.6 Evaluation metric.

By tracking the variation of RMSE and MAE with the number of incorporated features, the elbow rule is applied to identify the inflection point at which the error reduction transitions from steep to gradual. This inflection point is regarded as the minimal feature set required for reliable cross-domain SOH prediction, thereby enabling a quantitative evaluation of DE:

$$E_k = \frac{1}{2}(RMSE_k + MAE_k) \quad \text{(Equation 12)}$$

$$N_{elbow} = arg \max_{k \in \{1,\cdots,N\}} |E_{k+1} - 2E_k + E_{k-1}| \quad \text{(Equation 13)}$$

$$DE = N_{elbow} \quad \text{(Equation 14)}$$

Where, $E_k$represents the average error under the k-th feature subset, and N_{elbow}corresponds to the point with the maximum second-order difference, that is, the point where the error decline has the most obvious turning point.

XGBoost predictor

XGBoost is an optimized gradient-boosted decision tree algorithm designed for efficiency and scalability. The modeling logic of this algorithm can be described as follows: First, a generalized definition is given for the objective function. Then, in each iteration, a suitable regression tree is identified to fit the residual predicted in the previous iteration. Subsequently, by minimizing the objective function, the estimated value is progressively brought closer to the true value. It minimizes the following regularized objective function at each boosting iteration t:

$$\mathcal{L}^{(t)} = \sum_{\eta=1}^{n} l\left(y_\eta, \hat{y}_\eta^{(t-1)} + f_t(x_\eta)\right) + \Omega(f_t) \quad \text{(Equation 15)}$$

Where,n is the number of samples, y_η is the true SOH of sample η, $\hat{y}_\eta^{(t-1)}$ is the predicted SOH of sample η after t-1 iterations, $f_t(x_\eta)$ is the prediction from the t-th regression tree for input features x_η, $l(\cdot)$ is the loss function, and $\Omega(f_t)$ is the regularization term controlling model complexity, defined as:

$$\Omega(f_t) = \gamma T + \frac{1}{2}\lambda \sum_{j=1}^{T} \omega_\alpha^2 \quad \text{(Equation 16)}$$

Where T is the number of leaves in tree f_t, ω_α is the weight of leaf α, and γ and λ are regularization coefficients. To optimize $\mathcal{L}^{(t)}$, XGBoost uses a second-order Taylor expansion of the loss function around $\hat{y}_\eta^{(t-1)}$:

$$\mathcal{L}^{(t)} \approx \sum_{\eta=1}^{n} \left(l\left(y_\eta, \hat{y}_\eta^{(t-1)}\right) + g_\eta f_t(x_\eta) + \frac{1}{2} h_\eta f_t(x_\eta)^2 \right) + \Omega(f_t) \quad \text{(Equation 17)}$$

Where:

$$g_\eta = \frac{\partial l\left(y_\eta, \hat{y}_\eta^{(t-1)}\right)}{\partial \hat{y}_\eta^{(t-1)}} \quad \text{(Equation 18)}$$

$$h_\eta = \frac{\partial^2 l\left(y_\eta, \hat{y}_\eta^{(t-1)}\right)}{\partial \left(\hat{y}_\eta^{(t-1)}\right)^2} \quad \text{(Equation 19)}$$

The optimal tree structure and leaf weights are determined to minimize this approximate loss at each boosting step.

Transfer learning strategy

To address the challenge of limited labeled data in the target domain, a transfer learning strategy is employed, consisting of source-domain pretraining, target-domain fine-tuning, and subsequent prediction. In the first stage, the XGBoost model is trained on a source-domain dataset containing complete life cycle data, allowing it to learn general aging patterns from a rich feature set. Input features primarily include IC-derived descriptors, such as peak values, peak voltages, and integrated areas, while the number and type of features could be flexibly selected according to experimental design. In the second stage, the pretrained model is fine-tuned using only the first 25% of the target-domain labeled data. This procedure adjusts the model parameters to capture the specific aging behavior of the target batteries while retaining the general knowledge acquired from the source domain. Finally, the fine-tuned model is applied to estimate the SOH for the remaining 75% of the target-domain data, enabling continuous capacity trajectory reconstruction for unseen cycles.

The XGBoost model is configured with a maximum tree depth of 6, a learning rate of 0.05, subsampling and column subsampling rates of 0.8, and regularization to prevent overfitting. Pretraining is performed for 300 boosting rounds, followed by 100 additional rounds for fine-tuning. All model training and prediction procedures are implemented in Python using the XGBoost library.

Feature normalization

To ensure consistent scaling across domains, the features are standardized using Z score normalization. For transfer learning, the scaler is fitted jointly on the source-domain samples and the labeled portion of the target domain:

$$\mu, \sigma = StandardScaler.fit\left(X_{source} \cup X_{target}^{labeled}\right) \quad \text{(Equation 20)}$$

The obtained μ,σ is then applied to transform all source-domain samples for pretraining, the labeled target samples for fine-tuning, and the unlabeled target samples for final estimation:

$$\tilde{X}_{source} = \frac{X_{source} - \mu}{\sigma} \quad \text{(Equation 21)}$$

$$\tilde{X}_{target}^{labeled} = \frac{X_{target}^{labeled} - \mu}{\sigma} \quad \text{(Equation 22)}$$

$$\tilde{X}_{target}^{unlabeled} = \frac{X_{target}^{ulabeled} - \mu}{\sigma} \quad \text{(Equation 23)}$$

Evaluation metric

The *MAE* is defined as:

$$MAE = \frac{1}{C - d + 1} \sum_{j=d}^{C} |y_j - \hat{y}_j| \quad \text{(Equation 24)}$$

The *RMSE* is defined as:

$$RMSE = \sqrt{\frac{1}{C - d + 1} \sum_{j=d}^{C} (y_j - \hat{y}_j)^2} \quad \text{(Equation 25)}$$

The *MAPE* is defined as:

$$MAPE = \frac{\sum_{j=d}^{C} |y_j - \hat{y}_j|}{\sum_{j=d}^{C} y_j} \times 100\% \quad \text{(Equation 26)}$$

where y_j and $\hat{y}_j$ are the true SOH and estimated SOH in the jth cycle, respectively. C is the length of battery cycles, and d is the starting estimation point, which means the cycles used to fine-tune the source model.

DISCUSSION

This study systematically analyzes the predictive capability, transferable capability, and data efficiency of IC curve features for battery SOH estimation. The results show that the horizontal coordinates of IC peaks exhibit higher predictive capability, while vertical coordinates have higher transferability. Feature efficiency analysis reveals that features extracted from the first peak provide sufficient information for accurate estimation, achieving a favorable balance between prediction accuracy and testing cost. In addition, analysis of the source-battery efficiency indicates that two source batteries are adequate to achieve accurate transfer, while adding more batteries does not lead to improvements. These findings highlight the principle of data efficiency, suggesting that both the number of features and source batteries should be carefully selected to avoid unnecessary data collection and associated energy consumption.

Our findings align with previous studies that associate peak height variations in IC curves with the aging of electrode active materials and changes in lithium inventory, and link peak voltage shifts with increasing internal resistance.[43–47] While prior works focus on the physical interpretation of specific IC curve changes, our study confirms this understanding with data-driven predictive modeling by explicitly linking feature predictability and transferability to aging mechanisms. This confirms the physical significance of IC features while explaining why certain features, such as P1_x and P2_y, consistently demonstrate robustness across domains. The Pearson coefficient reflects the linear correlation between features, while the Spearman coefficient captures their monotonic relationship. The decrease in correlation between P1_x and P2_x under Spearman analysis indicates that their relationship is not strictly monotonic, possibly due to local peak shifts or measurement noise. In contrast, the increase in correlation between P1_y and P2_y suggests a more consistent monotonic degradation trend of reaction intensities during cycling.

Compared with earlier works that often rely on the full set of IC curve features or large amounts of training data, our study demonstrates that accurate and transferable SOH prediction can be achieved using a minimal and physically interpretable feature set, together with a limited number of source batteries. In this way, our work fills an important gap in the literature by establishing the concept of PC, TC, and DE of features in SOH estimation. This provides new insights into how to reduce the dependency on large datasets without compromising prediction reliability, which is particularly valuable under resource-constrained testing conditions.

The findings contribute to advancing the field by promoting a more efficient paradigm for battery health management, where feature selection and source-battery efficiency are guided by predictive performance and physical interpretability. The method remains applicable when the dataset changes, provided that the dataset includes batteries under different conditions that are transferable. This approach reduces testing costs and computational burdens and provides a framework for integrating domain knowledge with data-driven methods in a scalable manner.

From a practical standpoint, the concepts of PC, TC, and DE also provide valuable guidance for the design and deployment of battery management systems (BMSs). In real-world applications, BMSs are often constrained by limited computing power, restricted memory, and low sampling frequencies, particularly in embedded systems for electric vehicles or stationary storage. High-PC features enable accurate SOH estimation even when computational resources are limited, while high-TC features ensure that models trained under specific conditions remain reliable when applied to batteries experiencing different load patterns or environments. DE offers an accessible framework to balance sensing cost and prediction accuracy by identifying the minimal yet sufficient number of features and sampling points needed for reliable estimation, thereby reducing both data acquisition and communication burdens within the BMS.

Nevertheless, several limitations remain within this preliminary and demonstrative work since the current analysis is conducted under isothermal conditions; thus, the generalizability of the selected features under dynamic operating profiles or varying temperatures requires further validation. In addition, while the study focuses on handcrafted IC curve features, emerging approaches based on end-to-end deep learning may capture additional patterns beyond manually defined features. Future research should therefore extend this framework to non-isothermal and real-world cycling conditions, investigate the

integration of physically interpretable features with advanced machine learning models, and further explore data efficiency under broader transfer learning scenarios. In the era of increasingly large models and datasets,[48,49] our work emphasizes the importance of data efficiency, encouraging the development of methods that prioritize data quality and efficiency over sheer volume.

RESOURCE AVAILABILITY

Lead contact

Requests for further information and resources should be directed to and will be fulfilled by the lead contact, Shengyu Tao (shengyu.tao@chalmers.se).

Materials availability

No materials were used in this work.

Data and code availability

- All data used in this work can be found in the works of Chen et al.[41] and Zhu et al.[42] The supporting data are provided in the supplemental information.
- The modeling code and processed data have been deposited on GitHub at https://github.com/terencetaothucb/SOH-Estimation-Predictive-Capability-Transferable-Capability-and-Data-Efficiency-Analysis.git. The associated DOI is https://doi.org/10.5281/zenodo.17830907.
- All data are available in the main text and supplementary information. Any additional information required to reanalyze the data reported in this paper is available from the lead contact upon request.

ACKNOWLEDGMENTS

This work was supported by the Swedish Research Council through a Project Grant (grant no. 2023-04314), the European Union's Horizon Europe program through the Marie Skłodowska-Curie Actions (grant no. 101131278), the Key Scientific Research Support Project of Shanxi Energy Internet Research Institute (grant no. SXEI2023A002), and the Meituan Scholar Program-International Collaboration Project (grant no. 202209A).

AUTHOR CONTRIBUTIONS

L.S. and S.T. conceptualized, designed, reviewed, revised, and prepared the manuscript draft. Y.C., C.Z., and X.Z. supervised, reviewed, discussed, and acquired funding. All authors revised the manuscript before submission.

DECLARATION OF INTERESTS

The authors declare no competing interests.

SUPPLEMENTAL INFORMATION

Supplemental information can be found online at https://doi.org/10.1016/j.xcrp.2025.103083.

Received: September 21, 2025
Revised: November 17, 2025
Accepted: December 15, 2025

REFERENCES

1. Yu, P., Zhou, C., Yu, Y., Chang, Z., Li, X., Huang, K., Yu, J., Yan, K., Jiang, X., and Su, Y. (2025). Improved PSO-TCN model for SOH estimation based on accelerated aging test for large capacity energy storage batteries. J. Energy Storage *108*, 115031. https://doi.org/10.1016/j.est.2024.115031.
2. Li, X., Yuan, C., and Wang, Z. (2020). State of health estimation for Li-ion battery via partial incremental capacity analysis based on support vector regression. Energy *203*, 117852. https://doi.org/10.1016/j.energy.2020.117852.
3. Ma, L., Xu, Y., Zhang, H., Yang, F., Wang, X., and Li, C. (2022). Co-estimation of state of charge and state of health for lithium-ion batteries based on fractional-order model with multi-innovations unscented Kalman filter method. J. Energy Storage *52*, 104904. https://doi.org/10.1016/j.est.2022.104904.
4. Cao, N., Du, H., Lu, J., Li, Z., Qiang, Q., and Lu, H. (2025). Designing ionic liquid electrolytes for a rigid and Li+-conductive solid electrolyte interface in high performance lithium metal batteries. Chem. Phys. Lett. *866*, 141959. https://doi.org/10.1016/j.cplett.2025.141959.
5. Zou, Y., Lin, Z., Li, D., and Liu, Z. (2023). Advancements in Artificial Neural Networks for health management of energy storage lithium-ion batteries: A comprehensive review. J. Energy Storage *73*, 109069. https://doi.org/10.1016/j.est.2023.109069.
6. Gong, J., Xu, B., Chen, F., and Zhou, G. (2025). Predictive modeling for electric vehicle battery state of health: A comprehensive literature review. Energies *18*, 337. https://doi.org/10.3390/en18020337.
7. Pradhan, S.K., and Chakraborty, B. (2022). Battery management strategies: An essential review for battery state of health monitoring techniques. J. Energy Storage *51*, 104427. https://doi.org/10.1016/j.est.2022.104427.
8. Li, D., Yang, D., Li, L., Wang, L., and Wang, K. (2022). Electrochemical impedance spectroscopy based on the state of health estimation for lithium-ion batteries. Energies *15*, 6665. https://doi.org/10.3390/en15186665.
9. Liu, B., Tang, X., and Gao, F. (2020). Joint estimation of battery state-of-charge and state-of-health based on a simplified pseudo-two-dimensional model. Electrochim. Acta *344*, 136098. https://doi.org/10.1016/j.electacta.2020.136098.
10. Li, C., Yang, L., Li, Q., Zhang, Q., Zhou, Z., Meng, Y., Zhao, X., Wang, L., Zhang, S., Li, Y., and Lv, F. (2024). SOH estimation method for lithium-ion batteries based on an improved equivalent circuit model via electrochemical impedance spectroscopy. J. Energy Storage *86*, 111167. https://doi.org/10.1016/j.est.2024.111167.
11. Wu, C., Wang, L., Meng, J., Huang, J., Yang, T., Wang, L., Chang, Y., and He, X. (2025). A hybrid deep learning model for lithium-ion battery state-of-health estimation using electrochemical impedance spectroscopy. Energy *339*, 138974. https://doi.org/10.1016/j.energy.2025.138974.
12. Liu, Y., Yang, L., Liao, R., Hu, C., Xiao, Y., He, C., Wu, X., Zhang, Y., and Li, S. (2025). Degradation mechanism of sodium-ion batteries and state of health estimation via electrochemical impedance spectroscopy under temperature disturbances. Energy *332*, 137064. https://doi.org/10.1016/j.energy.2025.137064.
13. Tong, L., Li, Y., Xu, Y., Fang, J., Wen, C., Zheng, Y., Zhang, H., Peng, B., Yang, F., Zhang, J., and Gong, M. (2025). A combined method for state-of-charge estimation for lithium-ion batteries based on IGWO-ASRCKF and ELM under various aging levels. J. Energy Storage *124*, 116843. https://doi.org/10.1016/j.est.2025.116843.
14. Dubarry, M., Truchot, C., and Liaw, B.Y. (2012). Synthesize battery degradation modes via a diagnostic and prognostic model. J. Power Sources *219*, 204–216. https://doi.org/10.1016/j.jpowsour.2012.07.016.
15. Dawkins, J.I.G., Martens, I., Danis, A., Beaulieu, I., Chhin, D., Mirolo, M., Drnec, J., Schougaard, S.B., and Mauzeroll, J. (2023). Mapping the total lithium inventory of Li-ion batteries. Joule *7*, 2783–2797. https://doi.org/10.1016/j.joule.2023.11.003.
16. Wu, Z., Wang, H., and Zhang, Y. (2025). Mechanism-traced diagnosis of lithium inventory loss for lithium-ion batteries using physics-driven machine learning. Energy *338*, 138936. https://doi.org/10.1016/j.energy.2025.138936.

17. O'Kane, S.E.J., Ai, W., Madabattula, G., Alonso-Alvarez, D., Timms, R., Sulzer, V., Edge, J.S., Wu, B., Offer, G.J., and Marinescu, M. (2022). Lithium-ion battery degradation: how to model it. Phys. Chem. Chem. Phys. *24*, 7909–7922. https://doi.org/10.1039/D2CP00417H.

18. Weng, C., Cui, Y., Sun, J., and Peng, H. (2013). On-board state of health monitoring of lithium-ion batteries using incremental capacity analysis with support vector regression. J. Power Sources *235*, 36–44. https://doi.org/10.1016/j.jpowsour.2013.02.012.

19. Zhang, Z., Li, L., Li, X., Hu, Y., Huang, K., Xue, B., Wang, Y., and Yu, Y. (2022). State-of-health estimation for the lithium-ion battery based on gradient boosting decision tree with autonomous selection of excellent features. Int. J. Energy Res. *46*, 1756–1765. https://doi.org/10.1002/er.7292.

20. Tao, S., Ma, R., Chen, Y., Liang, Z., Ji, H., Han, Z., Wei, G., Zhang, X., and Zhou, G. (2024). Rapid and sustainable battery health diagnosis for recycling pretreatment using fast pulse test and random forest machine learning. J. Power Sources *597*, 234156. https://doi.org/10.1016/j.jpowsour.2024.234156.

21. Hu, C., Jain, G., Schmidt, C., Strief, C., and Sullivan, M. (2015). Online estimation of lithium-ion battery capacity using sparse Bayesian learning. J. Power Sources *289*, 105–113. https://doi.org/10.1016/j.jpowsour.2015.04.166.

22. Liu, K., Hu, X., Wei, Z., Li, Y., and Jiang, Y. (2019). Modified Gaussian process regression models for cyclic capacity prediction of lithium-ion batteries. IEEE Trans. Transp. Electrific. *5*, 1225–1236. https://doi.org/10.1109/TTE.2019.2944802.

23. Zheng, Y., Hu, J., Chen, J., Deng, H., and Hu, W. (2023). State of health estimation for lithium battery random charging process based on CNN-GRU method. Energy Rep. *9*, 1–10. https://doi.org/10.1016/j.egyr.2022.12.093.

24. Teixeira, R.S.D., Calili, R.F., Almeida, M.F., and Louzada, D.R. (2024). Recurrent neural networks for estimating the state of health of lithium-ion batteries. Batteries *10*, 111. https://doi.org/10.3390/batteries10030111.

25. Ma, Y., Shan, C., Gao, J., and Chen, H. (2022). A novel method for state of health estimation of lithium-ion batteries based on improved LSTM and health indicators extraction. Energy *251*, 123973. https://doi.org/10.1016/j.energy.2022.123973.

26. Peng, S., Wang, Y., Tang, A., Jiang, Y., Kan, J., and Pecht, M. (2025). State of health estimation joint improved grey wolf optimization algorithm and LSTM using partial discharging health features for lithium-ion batteries. Energy *315*, 134293. https://doi.org/10.1016/j.energy.2024.134293.

27. Che, Y., Deng, Z., Li, P., Tang, X., Khosravinia, K., Lin, X., and Hu, X. (2022). State of health prognostics for series battery packs: A universal deep learning method. Energy *238*, 121857. https://doi.org/10.1016/j.energy.2021.121857.

28. Wang, G., Li, C., Cui, Z., Yuan, H., and Cui, N. (2025). A practical state of health estimation method for lithium-ion batteries using charging duration in different voltage segments. J. Energy Storage *132*, 117712. https://doi.org/10.1016/j.est.2025.117712.

29. Wu, J., Fang, L., Dong, G., and Lin, M. (2023). State of health estimation of lithium-ion battery with improved radial basis function neural network. Energy *262*, 125380. https://doi.org/10.1016/j.energy.2022.125380.

30. Li, X., Yuan, C., Li, X., and Wang, Z. (2020). State of health estimation for Li-Ion battery using incremental capacity analysis and Gaussian process regression. Energy *190*, 116467. https://doi.org/10.1016/j.energy.2019.116467.

31. Lin, M., Wu, J., Meng, J., Wang, W., and Wu, J. (2023). State of health estimation with attentional long short-term memory network for lithium-ion batteries. Energy *268*, 126706. https://doi.org/10.1016/j.energy.2023.126706.

32. Zhao, J., Zhang, X., and Hu, C. (2025). Lithium-ion battery State-of-Health estimation using voltage-position encoding CNN and Incremental Capacity Analysis with a novel smoothing parameter selection strategy. J. Energy Storage *130*, 117296. https://doi.org/10.1016/j.est.2025.117296.

33. Dubarry, M., Svoboda, V., Hwu, R., and Yann Liaw, B. (2006). Incremental capacity analysis and close-to-equilibrium OCV measurements to quantify capacity fade in commercial rechargeable lithium batteries. Electrochem. Solid State Lett. *9*, A454. https://doi.org/10.1149/1.2221767.

34. Li, Y., Stroe, D.-I., Cheng, Y., Sheng, H., Sui, X., and Teodorescu, R. (2021). On the feature selection for battery state of health estimation based on charging–discharging profiles. J. Energy Storage *33*, 102122. https://doi.org/10.1016/j.est.2020.102122.

35. Marri, I., Petkovski, E., Cristaldi, L., and Faifer, M. (2023). Comparing Machine Learning Strategies for SoH Estimation of Lithium-Ion Batteries Using a Feature-Based Approach. Energies *16*, 4423. https://doi.org/10.3390/en16114423.

36. Li, H., and Chen, C. (2025). Lithium-ion battery SOH prediction based on multi-dimensional features and multi-model feature selector. Energy *331*, 136844. https://doi.org/10.1016/j.energy.2025.136844.

37. Wei, Z., Li, Y., Sun, X., Liu, W., Liu, C., and Lu, H. (2025). SOH estimation of lithium-ion batteries based on multi-feature extraction and improved DLEM. J. Energy Storage *120*, 116460. https://doi.org/10.1016/j.est.2025.116460.

38. Xia, X., Chen, Y., Shen, J., Liu, Y., Zhang, Y., Chen, Z., and Wei, F. (2025). State of health estimation for lithium-ion batteries based on impedance feature selection and improved support vector regression. Energy *326*, 136135. https://doi.org/10.1016/j.energy.2025.136135.

39. Tao, S., Sun, C., Fu, S., Wang, Y., Ma, R., Han, Z., Sun, Y., Li, Y., Wei, G., Zhang, X., et al. (2023). Battery Cross-Operation-Condition Lifetime Prediction via Interpretable Feature Engineering Assisted Adaptive Machine Learning. ACS Energy Lett. *8*, 3269–3279. https://doi.org/10.1021/acsenergylett.3c01012.

40. Wang, J., Zhang, C., Zhang, L., Su, X., Zhang, W., Li, X., and Du, J. (2023). A novel aging characteristics-based feature engineering for battery state of health estimation. Energy *273*, 127169. https://doi.org/10.1016/j.energy.2023.127169.

41. Chen, B., Liu, Y., and Xiao, B. (2024). A novel hybrid neural network-based SOH and RUL estimation method for lithium-ion batteries. J. Energy Storage *98*, 113074. https://doi.org/10.1016/j.est.2024.113074.

42. Zhu, J., Wang, Y., Huang, Y., Bhushan Gopaluni, R., Cao, Y., Heere, M., Mühlbauer, M.J., Mereacre, L., Dai, H., Liu, X., et al. (2022). Data-driven capacity estimation of commercial lithium-ion batteries from voltage relaxation. Nat. Commun. *13*, 2261. https://doi.org/10.1038/s41467-022-29837-w.

43. Vásquez, F.A., Sara Gaitán, P., and Calderón, J.A. (2025). Comparative study of methodologies for SOH diagnosis and forecast of LFP and NMC lithium batteries used in electric vehicles. J. Energy Storage *105*, 114725. https://doi.org/10.1016/j.est.2024.114725.

44. Jiang, Y., Jiang, J., Zhang, C., Zhang, W., Gao, Y., and Guo, Q. (2017). Recognition of battery aging variations for LiFePO4 batteries in 2nd use applications combining incremental capacity analysis and statistical approaches. J. Power Sources *360*, 180–188. https://doi.org/10.1016/j.jpowsour.2017.06.007.

45. Liu, J., Duan, Q., Ma, M., Zhao, C., Sun, J., and Wang, Q. (2020). Aging mechanisms and thermal stability of aged commercial 18650 lithium ion battery induced by slight overcharging cycling. J. Power Sources *445*, 227263. https://doi.org/10.1016/j.jpowsour.2019.227263.

46. Liu, C., Wen, X., Zhong, J., Liu, W., Chen, J., Zhang, J., Wang, Z., and Liao, Q. (2022). Characterization of aging mechanisms and state of health for second-life 21700 ternary lithium-ion battery. J. Energy Storage *55*, 105511. https://doi.org/10.1016/j.est.2022.105511.

47. Tao, S., Zhang, M., Zhao, Z., Li, H., Ma, R., Che, Y., Sun, X., Su, L., Sun, C., Chen, X., et al. (2025). Non-destructive degradation pattern decoupling for early battery trajectory prediction via physics-informed learning. Energy Environ. Sci. *18*, 1544–1559. https://doi.org/10.1039/D4EE03839H.

48. Tao, S., Ma, R., Zhao, Z., Ma, G., Su, L., Chang, H., Chen, Y., Liu, H., Liang, Z., Cao, T., et al. (2024). Generative learning assisted state-of-health estimation for sustainable battery recycling with random retirement conditions. Nat. Commun. *15*, 10154. https://doi.org/10.1038/s41467-024-54454-0.

49. Tao, S., Guo, R., Lee, J., Moura, S., Casals, L.C., Jiang, S., Shi, J., Harris, S., Zhang, T., Chung, C.Y., et al. (2025). Immediate remaining capacity estimation of heterogeneous second-life lithium-ion batteries via deep generative transfer learning. Energy Environ. Sci. *18*, 7413–7426. https://doi.org/10.1039/D5EE02217G.